

UNIVERSITY of CALIFORNIA  
SANTA CRUZ

**A *CHANDRA* X-RAY FOLLOW-UP TO THE DARK ENERGY  
SURVEY YEAR 3 *REDMAPPER* CATALOG**

A thesis submitted in partial satisfaction of the  
requirements for the degree of

BACHELOR OF SCIENCE

in

ASTROPHYSICS

by

**Lena Eiger**

30 August 2019

Copyright © by

Lena Eiger

2019

## Abstract

A *Chandra* X-Ray Follow-Up to the Dark Energy Survey Year 3 *redMaPPer* Catalog

by

Lena Eiger

Observations of galaxy clusters can provide constraints on the dark energy equation of state, since the cluster mass function is dependent on the amount of dark energy in the universe. While cluster mass is not observable directly, it can be related to various observables such as richness, which is similar to the number density of galaxies. We find the scaling relations between the richness observable in optical and two lower-scatter X-ray observables, X-ray luminosity ( $L_X$ ) and temperature ( $T_X$ ). We find scaling relations and intrinsic scatter distributions for richness from the Dark Energy Survey Year 3 Data Release (DES Y3) *redMaPPer* cluster catalog with corresponding X-ray temperatures and luminosities from archival *Chandra* images using the MATCha pipeline as introduced in Hollowood et al. (2018). We investigate offsets between X-ray and optical cluster centers in DES Y3 in order to correct for cluster mis-centering. In addition, we detail upgrades to the MATCha pipeline for increasing the depth of interpretable X-ray data and future core-cropped cluster analysis.

# Contents

List of Figures	v
List of Tables	vi
Dedication	vii
Acknowledgements	viii
<b>1 Introduction</b>	<b>1</b>
<b>2 Background</b>	<b>5</b>
2.1 The Dark Energy Survey and the <i>redMaPPer</i> algorithm . . . . .	5
2.2 X-ray Follow-Up of Optical Clusters and the <i>MATCha</i> Pipeline . . . . .	7
<b>3 Upgrades to the <i>MATCha</i> pipeline</b>	<b>13</b>
3.1 Iterative Algorithm for Finding Luminosities without Temperatures . . . . .	13
3.2 Implementation of Centering on X-ray Peaks . . . . .	15
3.3 Automated Chip-Edge Flagging . . . . .	15
<b>4 Results</b>	<b>16</b>
4.1 <i>MATCha</i> Sample for DES Y3 . . . . .	16
4.2 Scaling Relations . . . . .	17
4.2.1 $T_X - \lambda$ Scaling Relation . . . . .	18
4.2.2 $L_X - \lambda$ Scaling Relation . . . . .	20
4.3 Centering . . . . .	23
<b>5 Summary and Future Work</b>	<b>27</b>

# List of Figures

2.1	MATCha algorithm overlaid on an X-ray image . . . . .	12
3.1	Validation of Iterative Method for X-ray Luminosity . . . . .	14
4.1	Preliminary $r_{2500} T_X - \lambda$ scaling relation for DES Y3 clusters in the <i>Chandra</i> archival sample. . . . .	21
4.2	Previous results for $r_{2500} T_X - \lambda$ scaling relations. . . . .	22
4.3	Preliminary $r_{2500} L_X - \lambda$ scaling relation for DES Y3 clusters in the <i>Chandra</i> archival sample. . . . .	24
4.4	$r_{2500} L_X - \lambda$ scaling relation from Hollowood et al. (2018). . . . .	25
4.5	Centering histogram and corner plot for DES Y3 clusters. . . . .	26

# List of Tables

4.1	$r_{2500} T_X - \lambda$ scaling relations across multiple samples. . . . .	19
4.2	$r_{2500} L_X - \lambda$ scaling relations across multiple samples. . . . .	23
4.3	Fit parameters for centering gamma distributions across <i>redMaPPer</i> catalogs.	26

For Dr. Immel.

May this be another gold star.

## Acknowledgements

My deepest gratitude goes to my advisor, Professor Tesla Jeltema, for supporting me through this research and my time at UCSC. From teaching the very first physics class I took at UCSC to taking me to the Dark Energy Survey Collaboration Meeting to present this work, Tesla has always inspired me as an incredible scientist, a skilled leader, and a steadfast woman in physics. I will always be grateful for her commitment to maintaining a strong community of kind-hearted people. Her undying belief in me through even the most difficult moments has brought me strength that I will carry with me for my whole life.

I would be remiss not to thank my graduate student mentor Devon Hollowood, who brought me into the magical world of his X-ray analysis pipeline *MATCha*, with which much of this thesis is concerned. He has taught me much of what I know with unparalleled patience and understanding. I cherish the memories of our long talks about East Bay Hardcore Punk music after solving code issues on hot summer afternoons.

Much of my success is due to my dear friends and research group cohort Raziq Noorali and Brynn Hegland, who were with me from the beginning of this journey. Through hours of grueling homework, late-night emotional support phone calls, and multiple instances of classic Queer Brunch, the three of us crafted a community in an isolating and homogenous major. I hope that we continue to foster this community together through the coming years, whatever changes may come.

I would like to thank Spencer Everett and Sunayana Bhargava, both for the essential content and guidance they contributed to this work, as well as their support and friendship. From stressed-out python debugging to telephone pictionary, Spencer and Sunayana left a remarkable positive impact on my life during a difficult time.

My thanks also goes to Alex McDaniel and David Laubner, my indelible conference buddies, for helping me through presentations and of course for their warm friendship. I would like to thank Vernon Wetzell for his last-minute plotting help, his contribution to this work, and for his confidence in me through writing this thesis.

I would like to thank my friends and family: my parents Lenny and Vairagya Eiger, my grandmother Phyllis Eiger, and my dear friends Matthew Aguirre, Austin Schafer, Kris Palmer, Cibyl Engel, Luka Coole, Noah Dove, Lee Bernard, Sandra Nair, Zee Moffatt, Rona Berger, and Quentin Barth.

I would like to thank my mentor, Professor Enrico Ramirez-Ruiz, for his support and invaluable guidance. His warmth, generosity and deep understanding of the universe— as well as the lived experiences of others— will always be an inspiration to me.

I would like to thank The Box (Santa Cruz's weekly goth night), the Porter College Transfer Community, Trans-Inclusive Housing at Redwood Grove Apartments, the Lionel Cantu Queer Center, and the UCSC Disability Students' Union for giving me a sense of community outside of physics and allowing me a space to be my authentic self.

Finally, I would like to thank Carl Sagan for sparking my fascination with the beauty of the stars and Robert Smith of The Cure for keeping it alive in my heart.

# 1

## Introduction

Dark energy is currently conceptualized as a fluid with negative pressure which accelerates the universe's expansion. While the nature of dark energy remains a mystery, there are multiple techniques for constraining its equation of state. The discovery that the universe is expanding at an accelerating rate used Type 1a supernovae as standard candles (Riess et al., 1998; Perlmutter et al., 1999); however, observations of galaxy clusters can also be used to constrain cosmological parameters and provide evidence for accelerated cosmic expansion. Because galaxy clusters are the largest gravitationally bound structures in the universe, their abundance can tell us a lot about dark energy. For example, if dark energy had been dominant at early times, galaxy cluster formation would have had to begin earlier to explain their current density. Therefore, observations of the number density of galaxy clusters across redshift as a function of mass (known as the “mass function”) can offer insight into how much dark energy was present in the universe through time (Vikhlinin et al., 2009).

The number density of galaxy clusters is a function of each cluster's total mass,

so in order to use galaxy clusters to constrain cosmological parameters, one must find the cluster mass. Galaxy clusters are made up of three main components: galaxies, dark matter, and gas. Gas (and, indirectly, dark matter) can be observed using X-ray observations, whereas galaxies can be observed in optical surveys. Given the difficulty of measuring the mass of a galaxy cluster directly, other observable quantities which are correlated with cluster mass have to be used as “mass proxies.” For example, the number of galaxies in a cluster and the brightness of the gas emission in X-ray are both observables that correlate with mass. Each mass-observable relation has an intrinsic scatter, and so it’s imperative to quantify this scatter. In this thesis, I detail methods to better constrain the richness observable, a measure of galaxy content as defined in Rozo et al. 2009, and its intrinsic scatter distribution, as well as methods for correcting the mis-centering of galaxy clusters in order to better constrain cosmological parameters. This project investigates observable-mass relations from both optical and X-ray data; in particular, those concerning the observables cluster richness ( $\lambda$ ) as well as X-ray luminosity ( $L_X$ ) and temperature ( $T_X$ ). Most cosmological studies of galaxy clusters employ a method called “stacked weak lensing” (described in **Section 2.1**) to deduce mean observable-mass relations; however, these studies do not give an “intrinsic scatter,” or error estimate, on scaling relations. In addition, observable-mass relations from stacked weak lensing analyses are particularly susceptible to errors from miscalculated centers (Melchior et al., 2017), and therefore it is necessary to study multiple observables so as to deduce intrinsic scatter for observables and to correct miscalculated cluster centers.

In order to better understand the intrinsic scatter of the richness observable  $\lambda$  and calibrate galaxy cluster centers, Hollowood et al. (2018) introduced the **Mass Analysis**

**Tool for Chandra (*MATCha*).** *MATCha* uses archival *Chandra* telescope exposures to find the corresponding X-ray luminosities and temperatures of *redMaPPer* clusters in catalogs such as the Sloan Digital Sky Survey Data Release 8 (SDSS DR8) *redMaPPer* catalog. Using temperature-richness and luminosity-richness scaling relations, we deduce intrinsic scatter distributions between richness  $\lambda$  and *MATCha*'s output X-ray temperatures and luminosities. In addition, *MATCha*'s output X-ray peaks and centroids allow us to correct for mis-centering in *redMaPPer* cluster catalogs, which has been performed on the SDSS DR8 and the Dark Energy Survey Year 1 (DES Y1) *redMaPPer* catalogs (Hollowood et al., 2018; Zhang et al., 2019).

This thesis details notable upgrades to the *MATCha* pipeline, as well as analysis of the Dark Energy Survey Year 3 (DES Y3) Data Release. Firstly, we upgrade *MATCha*'s fitting algorithm such that it's possible to find an  $L_X$  value when no  $T_X$  can be calculated from available data. Luminosities found using this algorithm do not deviate from luminosity values fit alongside a known  $T_X$ . Secondly, we integrate X-ray peak finding into the *MATCha* pipeline, and introduce centering on the X-ray peak of galaxy clusters. This allows us to avoid problems with clusters whose centroid is offset from their cluster cores. In the future, it will allow core cropped analysis of clusters as in Vikhlinin et al. (2006). We lay the groundwork for automatic calculation of the fraction of the X-ray cluster source and background which lie within *Chandra*'s field of view. Finally, we repeat the analysis detailed in Hollowood et al. (2018) on DES Y3 clusters, finding a  $T_X - \lambda$  relation of  $\ln(E(z)^{-2/3}kT_X) = (0.36 \pm 0.05) \ln(\lambda/67.11) + (1.91 \pm 0.02)$  with intrinsic scatter of  $\sigma_{intr} = 0.28 \pm 0.02$  and an  $L_X - \lambda$  relation of  $\ln(L_X)/E(z) = (1.09 \pm 0.09) \ln(\lambda/67.11) + (0.18 \pm 0.06)$  with intrinsic scatter of  $\sigma_{intr} = 0.85 \pm 0.01$ . We repeat centering analysis detailed in Zhang

et al. (2019), and find a well-centered fraction for DES Y3 of  $0.779^{+0.048}_{-0.100}$ .

## 2

# Background

### 2.1 The Dark Energy Survey and the *redMaPPer* algorithm

The Dark Energy Survey (DES) is an optical and near-infrared survey of 5000 square degrees of the southern hemisphere in *griz* bands (as in the Sloan Digital Sky Survey), using a 3 square degree CCD camera mounted on the Blanco 4m Cerro Telolo Inter-American Observatory. Over its five years of observation the Dark Energy Survey has analyzed approximately 300 million galaxies (The Dark Energy Survey Collaboration, 2005). This project focuses on analysis of galaxy clusters from the first three years of observation, which was released to the collaboration in June 2018. Data from more recent years is yet to be released.

Clusters in large surveys such as DES can be detected and analyzed using cluster-finding algorithms. While finding an object's equatorial coordinates from an image is fairly straightforward, estimating the redshift of an object is much more complicated, and must be performed cleverly. This analysis employs the **red**-sequence **M**atched-filter **P**robabilistic

**Percolation** (*redMaPPer*) cluster finder, introduced in Rykoff et al. (2014). Galaxies which belong to one cluster reside at the same redshift, which gives them similar color. Given that most cluster galaxies are old and therefore comprised of mostly red stars (Bell et al., 2004), clusters are mostly red in optical data, and one can thus extrapolate the redshift of cluster galaxies from photometric data alone (Rykoff et al., 2014). The *redMaPPer* cluster finding algorithm detects galaxy clusters based on a minimal sample of optical spectroscopic data on red-sequence galaxies, and outputs their richness  $\lambda$  as well as the locations of their centers (Rykoff et al., 2016) in cluster catalogs that can be used in cosmological studies.

Richness is an optical cluster observable which is analogous to the number of red (“red-sequence”) galaxies within a cluster. While many optical cluster observables have been called “richness” in the past, the richness calculated by *redMaPPer* is the total membership probability of all red-sequence galaxies within the cluster. Richness scales with mass with relatively low intrinsic scatter, and is therefore a powerful optical cluster observable. However, the intrinsic scatter distribution of richness with mass is not well-understood.

Observable-mass relations can be determined from optical cluster data using stacked weak lensing (Leauthaud et al., 2010; Simet et al., 2017). The only way to directly observe the mass of a large object such as a galaxy cluster involves measuring how much its gravitational pull bends the light from surrounding objects in a phenomenon known as “gravitational lensing.” While large cosmological surveys often do not have the depth of data to infer mass based on gravitational lensing alone, the process of “stacking,” multiple similar clusters on their centers and averaging their properties can produce reasonable average masses and therefore mean observable-mass relations such as the ones relating the observables dis-

cussed above. However, observable-mass relations from stacked weak lensing analyses are particularly susceptible to errors from miscalculated centers (Melchior et al., 2017), and therefore it is necessary to study multiple observables so as to correct miscalculated cluster centers.

In this study, we investigate the intrinsic scatter of  $\lambda$  with mass using analysis of X-ray images from the *Chandra* X-ray Observatory of clusters found in the DES Y3 *redMaPPer* catalog, and use centers calculated from these X-ray clusters to calibrate for cluster mis-centering in *redMaPPer* catalogs.

## 2.2 X-ray Follow-Up of Optical Clusters and the *MATCha* Pipeline

One way to constrain the intrinsic scatter of optical cluster observables is by following up observations in other wavelengths. Following up optical cluster catalogs with X-ray data is ideal for three reasons: the availability of archival *Chandra* data on hundreds of clusters in optical cluster catalogs, the existence of low-scatter X-ray mass proxies, and that the presence of X-ray emission closely follows the density of clusters, so that their centers can be easily picked out. In addition, there is already a precedent for using X-ray temperature to understand the intrinsic scatter of richness as in Rozo & Rykoff (2014).

The X-ray luminosity ( $L_X$ ) and temperature ( $T_X$ ) are powerful follow-up observables because they can be measured from the X-ray flux and the X-ray spectrum respectively.  $L_X$  is observable through a phenomenon known as Bremsstrahlung radiation, in which electrons are slowed down by positively charged nuclei in the intracluster medium (ICM) and

emit light which is detectable in X-ray frequencies. Cluster luminosity is proportional to the square of the electron density in cluster gas.  $T_X$  can be inferred from the cluster's X-ray spectrum. Both observables relate to properties of the cluster gas. Because gas is mostly in hydrostatic equilibrium in the cluster potential well, both of these properties can tell us about the depth of the cluster potential well and therefore about cluster mass.

We use the **Mass Analysis Tool for Chandra** (*MATCha*, Hollowood et al. (2018)) to follow up clusters which appear in both *redMaPPer* optical catalogs and the *Chandra* archive. *MATCha* is an automated, massively parallelized pipeline which takes a set of equatorial coordinates (RA, Dec) and a redshift ( $z$ ), from a *redMaPPer* cluster catalog. Using these, it automatically downloads any *Chandra* images at these coordinates and attempts to find  $T_X$  and  $L_X$ , cluster centroids and X-ray peaks, and  $r_{2500}$  and  $r_{500}$  radii. The centroid is defined as the center of surface brightness of an observation within a region.  $r_{2500}$  is the radius around a galaxy cluster halo within which the density is 2500 times the critical density of the universe, and  $r_{500}$  is the radius around a cluster halo within which the density is 500 times the critical density of the universe. These calculations are performed at once on different cores of a supercomputer, and *MATCha* is structured to optimize for such an environment, storing previously-run analyses in a cache so as to avoid duplicate calculations. In order to perform its analysis, *MATCha* uses a series of CIAO and HEASOFT tools (Fruscione et al., 2006).

*MATCha*'s first step in X-ray follow-up of optical clusters is to find as many clusters as possible in archival *Chandra* data. It does so by querying the *Chandra* database for sky coordinates given in a *redMaPPer* catalog using a CIAO tool called *find\_chandra\_obsid*. For each set of coordinates in a *Chandra* observation, *MATCha* downloads the *Chandra* images

and processes them using the CIAO tool *chandra\_repro*, which runs the recommended set of *Chandra* data processing steps. *MATCha* then narrows the energy range to 0.3-7.9keV and removes particle background flares using the CIAO tool *deflare* before creating images and exposure maps for each observation. Finally, *MATCha* identifies point sources in the images using the CIAO tool *wavdetect* and removes them from the observation. This concludes the data processing step, after which *MATCha* begins the attempt to find X-ray centroids, temperatures and luminosities.

The algorithm for determining  $L_X$ ,  $T_X$ , centroids,  $r_{2500}$  and  $r_{500}$  is intensive. In general,  $T_X$  is found using the CIAO tool *XSPEC* to fit a temperature to the X-ray spectrum in each observation. This is done assuming a galactic hydrogen column density from the HEASOFT tool *nH*.  $L_X$  is then calculated from the flux and the distance to the cluster. Centroids are calculated using the CIAO tool *dmstat*, iteratively and initially within a 500kpc region. If a  $T_X$  can be found within a 500kpc aperture, an  $r_{2500}$  radius is calculated from this  $T_X$  using the scaling relation in Arnaud et al. (2005). A new centroid is calculated within the  $r_{2500}$  radius, and  $T_X$  and  $L_X$  are found within this region. This is repeated for the  $r_{500}$  radius.

An outline of the *MATCha* algorithm is as follows: First, *MATCha* centers a 500kpc region around the *redMaPPer* position. It then iterates centering by moving the 500kpc radius aperture for 20 iterations or if the new center is within 15kpc of the old center. If 20 iterations are reached, the cluster is marked as “undetected.” If *MATCha* is able to iterate until convergence within 15kpc, it then checks whether the signal-to-noise ratio (SNR) for the source region is greater than 5.0. If not, this cluster is also marked as “undetected.”

For undetected clusters, upper limits on  $L_X$  are calculated from an assumed temperature of 3.0 keV and an assumed  $r_{2500}$  of 500 kpc.

For “detected” clusters, *MATCha* extracts a background-subtracted spectrum within a 500 kpc aperture and uses this to fit  $T_X$  and  $L_X$  within 500 kpc. If the spectral fit fails to find a  $T_X$ , *MATCha* iterates on the  $L_X - T_X$  relation with a starting assumed temperature of 3.0 keV until values converge within uncertainty, with maximum iterations set to 10. If the spectral fit is successful, an  $r_{2500}$  region and centroid is then calculated from the 500 kpc  $T_X$ . These steps are repeated for the  $r_{500}$  region.

X-ray peaks are found by smoothing the binned *Chandra* image and then finding the brightest pixel within 500 kpc of the 500 kpc centroid found previously. The location of the X-ray peak is checked (and, rarely, corrected) visually as a crucial part of post-pipeline analysis.

After the  $L_X$ ,  $T_X$ , centroids and X-ray peaks are found using *MATCha*, the sample is filtered both for potential problems with the automated analysis and for interesting cluster properties. The first step in this post-pipeline analysis is to check that no detected clusters are actually bright nearby clusters rather than the intended *redMaPPer* cluster, which may lie in the foreground or background of an image of a bright nearby object. This is done by comparing the output cluster catalog to the catalog in the NASA/IPAC Extragalactic Database (NED) (NASA/IPAC Extragalactic Database, 2019). Then, the images are examined visually.

The first set of criteria marked by the research group falls broadly into the category of problems which inhibit accurate measures of data. These include instances in which most of the cluster source or background regions are not in *Chandra*’s field of view, or if *Chandra*

was not in an imaging mode when all images were taken. These clusters are cut from the sample. For undetected clusters, the post-pipeline flagging ends here, as images of them are not often clear, and they are only used as upper limits in  $L_X$ - $\lambda$  scaling relations. Clusters in which a significant portion of the background or source is obscured or contaminated by a nearby cluster are also flagged to be cut from the dataset. These clusters are flagged as “overlap.” Clusters which are incorrectly identified by *MATCha* as a *redMaPPer* cluster but are in fact a cluster in the foreground or background of the *redMaPPer* cluster are marked as “masked,” and also cut from the sample.

The second set of criteria fall into the category of interesting cluster attributes. Clusters undergoing mergers are perhaps the most obvious to identify; however, “serendipitous” clusters are also identified. Serendipitous clusters are defined as clusters which were not the aimpoint of the *Chandra* observation. These are interesting because they do not suffer the same selection bias as the rest of the archival sample: while images that have been taken for other studies are biased towards bright, dynamic clusters with peculiar astrophysics, serendipitous clusters – clusters which were not selected to be observed at all – are free from this bias.

A visual representation of *MATCha* run on a typical cluster is shown in **Fig. 2.1**, which shows the X-ray peak, *redMaPPer* center, 500kpc,  $r_{2500}$ , and  $r_{500}$  regions overlaid on an X-ray image of a *redMaPPer* cluster from the *Chandra* archive. *MATCha* and the methods described above have been used in several previous works; notably in an analysis of clusters in the Sloan Digital Sky Survey Data Release 8 *redMaPPer* catalog (Hollowood et al., 2018) and the Dark Energy Survey Year 1 *redMaPPer* catalog (Farahi et al., 2019). *MATCha*’s centering analysis has been used in Zhang et al. (2019).

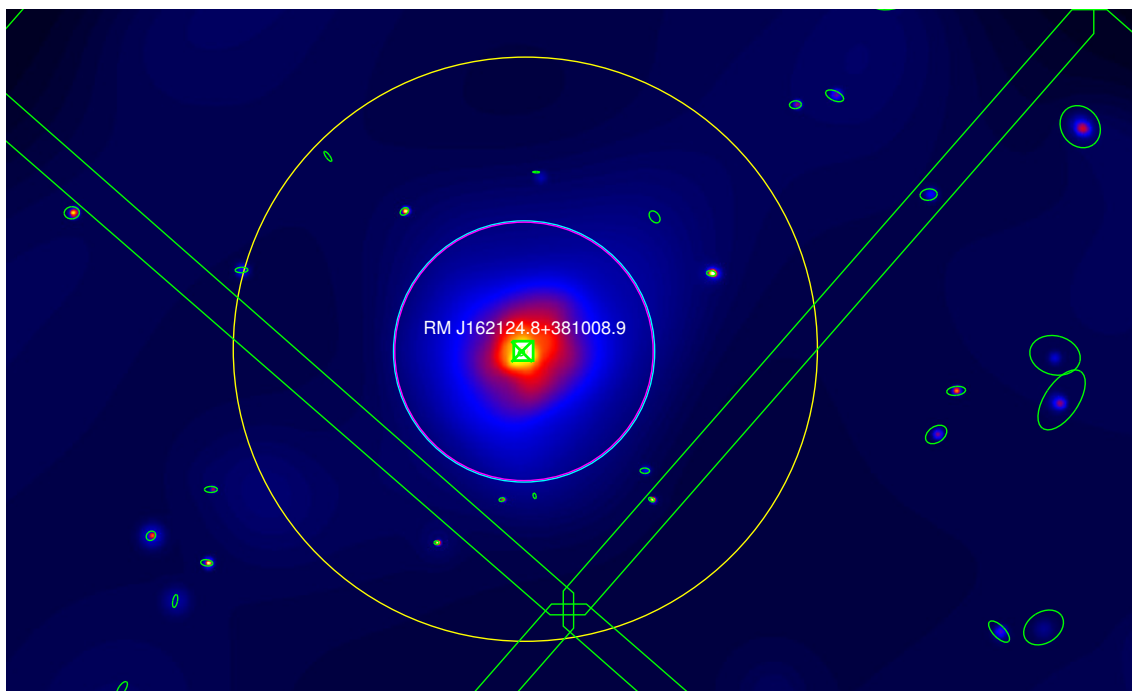


Figure 2.1: MATCha output: an archival Chandra exposure of redMaPPer cluster J162124.8+381008.9. The green squares mark the edges of Chandra’s CCD chips. The white dot marks the location of the redMaPPer cluster, whereas the green “x” marks the location of the X-ray peak as detected by MATCha. The pink circle marks the 500 kpc radius. The cyan circle is the  $r_{2500}$  radius, or the radius in which cluster mass density is 2500 times the critical density of the universe, and the yellow circle is the  $r_{500}$  radius, or the radius in which cluster mass density is 500 times the critical density of the universe. The gradient shown around the cluster is x-ray intensity; the dimmer signals are blue, whereas the brightest points of the cluster show in orange and yellow to white. Green ellipses indicate point sources which are removed from the analysis.

### 3

## Upgrades to the *MATCha* pipeline

While this thesis is primarily concerned with scaling relation and centering results for DES Y3 using *MATCha*, much of my work has been on improving the *MATCha* pipeline itself. This section details methods which have been improved by my own work.

### 3.1 Iterative Algorithm for Finding Luminosities without Temperatures

We find cluster X-ray luminosity  $L_X$  via X-ray flux and redshift distance. However, in order to infer the X-ray flux, it is necessary to have information on the X-ray spectrum and thus the energy distribution of photons. With deep enough data,  $T_X$  can be fit alongside a spectral model (in this case, we use Bremsstrahlung and line emission), which requires that data have enough photons to sample the shape of the spectrum so they can be fit to a model and a  $T_X$ . There exists a considerable fraction of our sample for which the depth of data is not sufficient to fit the temperature from the X-ray spectrum.

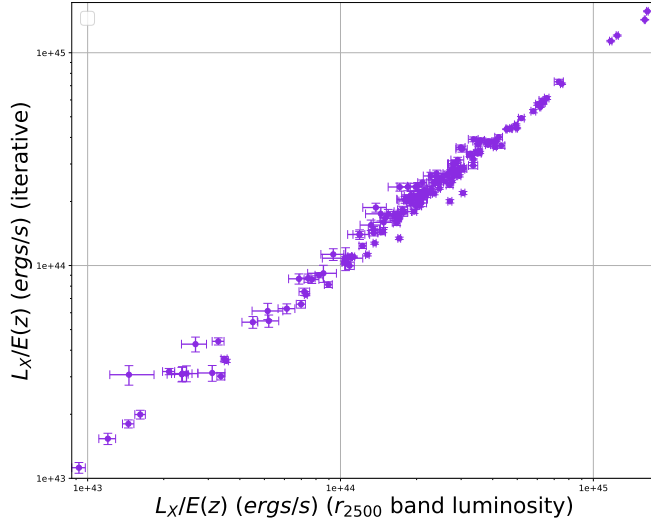


Figure 3.1:  $L_X$  found from iteration on  $L_X - T_X$  relation vs. measured  $L_X$  values (all points had both an iteratively calculated  $L_X$  and an  $L_X$  which was fit alongside  $T_X$ ). Note how these follow a one-to-one relation across luminosity, which becomes tighter as  $L_X$  values increase.

Within typical values of  $T_X$ ,  $L_X$  is more dependent on the normalization of the X-ray spectrum than its shape. Therefore, by assuming a  $T_X$  typical of the low-richness clusters which do not offer deep enough data to fit  $L_X$  alongside  $T_X$ , we can get a value of  $L_X$  which is within a factor of 2 of the actual value. Elaborating on this, we can assume a  $T_X$  value to start with, calculate a corresponding  $L_X$ , and iterate on the  $L_X - T_X$  scaling relation until convergence. As shown in in **Figure 3.1**, luminosities found using this method are not shown to deviate significantly from measured luminosities. This algorithm has been implemented in the *MATCha* pipeline and used in the  $L_X - \lambda$  scaling relation in **Section 4.2**.

### 3.2 Implementation of Centering on X-ray Peaks

Implementation of centering on the X-ray peak was considerably more straightforward because the X-ray peak can be calculated using the CIAO tool *dmstat*. While previously, X-ray peaks were found using a python post-processing tool, centering analysis on the X-ray peak required peak finding to be integrated into the main pipeline. First, images are created and exposure corrected from each observation using *fluximage*. Then, the image was smoothed around the X-ray peak using the CIAO tool *aconvolve* and a 2D Gaussian function with a 50kpc radius. Then, *dmstat* was run on the smoothed, exposure-corrected image to get the maximum-valued pixel. These steps are performed on every observation of any cluster in given a region. Core-cropped  $L_X$  values have shown to have lower scatter, so this method will be useful in future analyses, and will also enable analysis of cool cores in our cluster sample.

### 3.3 Automated Chip-Edge Flagging

Some of the visual analysis described in Section 2.2 can be quantified numerically. Therefore, it can be automated, which saves time and increases consistency. Specifically, one can already calculate the fraction of an aperture which lies outside the field-of-view; the CIAO tool *dmstat* already outputs this value with each run as “good” and “null” pixels. Work on quantifying an acceptable good/null pixel ratio such that source and background regions of each cluster we analyze lie within *Chandra*’s field of view is being done right now by a current undergraduate, Jose Jobel, with my guidance.

## 4

# Results

### 4.1 *MATCha* Sample for DES Y3

The sample used in the fit for  $T_X - \lambda$  consists of detected clusters in the Dark Energy Survey Year 3 *redMaPPer* catalog and the *Chandra* archive for which  $T_X$  could be fit from the X-ray spectrum, and which were not flagged as masked, bad mode, or as having any significant portion of the cluster or background on a chip edge. Of the 53,610 clusters in the DES Y3 *redMaPPer* catalog, 1092 could be found in *Chandra* archival data. Of these, 321 were marked as “detected” (signal-to-noise ratio  $> 5$ ). Of these, there remained 163 clusters which did not have the above-mentioned flags. This sample is smaller than the SDSS DR8 *redMaPPer* sample used for both the  $T_X - \lambda$  and  $L_X - \lambda$  scaling relations in Hollowood et al. (2018) (235 clusters) and over twice the sample used for both the  $T_X - \lambda$  and  $L_X - \lambda$  scaling relations for DES Y1 in Farahi et al. (2019) (68 clusters). The sample used in the fit for  $L_X - \lambda$  for DES Y3 consists of detected clusters in the DES Y3 *redMaPPer* catalog and the *Chandra* archive for which luminosities could be fit or calculated, and without the

same flags mentioned above. Of the 321 detected clusters, there remained 237 clusters for which the  $r_{2500}$  luminosity could be fit or iteratively calculated. This is nearly 4 times as large of a sample as the sample from DES Y1, and comparable to the sample from SDSS DR8. It is no mystery that the sample which could be used for the  $L_X - \lambda$  scaling relation was much larger than the  $T_X - \lambda$  sample, as the methods outlined in **Section 3.1** enabled the inclusion of 74 additional clusters. The luminosity used in this study was the  $r_{2500}$  soft band luminosity (0.5-2 keV).

The centering sample consisted of detected clusters not flagged as masked, bad mode, or having an X-ray peak on a chip edge, for which the signal-to-noise ratio in a 500kpc radius was greater than 10. Of the 321 detected clusters, 174 had a signal-to-noise ratio greater than 10 and did not have the above flags. This is over twice the sample size for DES Y1 *redMaPPer*-selected clusters in the *Chandra* archive (67) and comparable to the sample size for SDSS DR8 *redMaPPer*-selected clusters in the *Chandra* archive (144), despite that a less conservative cut on signal-to-noise ratio was made on these samples (Zhang et al., 2019).

## 4.2 Scaling Relations

Linear regressions for  $T_X - \lambda$  and  $L_X - \lambda$  scaling relations were performed using a hierarchical Bayesian model as in Kelly (2007) implemented in the CluStR fitting code by Spencer Everett and Vernon Wetzell. We compare our results to the DES Y1 *redMaPPer* sample which appears in *Chandra* data in Farahi et al. (2019) and the SDSS DR8 *redMaPPer* sample which appears in *Chandra* data in Hollowood et al. (2018). Our methods for fitting both  $T_X - \lambda$  and  $L_X - \lambda$  scaling relations follow those in Hollowood et al. (2018) for  $r_{2500}$

$T_X$  and  $L_X$  across all redshifts. Our results differ from *Chandra* results in Farahi et al. (2019) in that their values for  $\lambda$  were recalculated at the X-ray peak of each cluster, which lessens the intrinsic scatter on the relation due to cluster mis-centering. Therefore it is reasonable that the intrinsic scatter in this thesis should be comparable to Hollowood et al. (2018) and more than in Farahi et al. (2019). Scaling relations are presented in the form  $y = \alpha \ln(\lambda/\lambda_{piv}) + \beta$ , where  $\lambda_{piv}$  is the pivot point of the fit and  $y$  is a normalized X-ray observable  $T_X$  or  $L_X$ .

#### 4.2.1 $T_X - \lambda$ Scaling Relation

The  $T_X - \lambda$  scaling relation is normalized by the factor  $E(z)^{-2/3}k$ , where  $E(z) = H(z)/H_0$  is the evolution of the Hubble parameter with redshift and  $k$  is Boltzmann's constant. If we assume that clusters are self-similar and in hydrostatic equilibrium, we can expect the quantity  $E(z)^{-2/3}kT_X$  to correlate more strongly with mass than  $T_X$  alone (Kaiser, 1991), as  $E(z)$  accounts for cluster evolution with redshift across a broad redshift range. Therefore, we fit the  $E(z)^{-2/3}kT_X - \lambda$  scaling relation. Our fitting algorithm sets  $\lambda_{piv}$  to the median of  $\lambda$ , which in this sample was 67.11. Fit parameters for the  $r_{2500} T_X - \lambda$  scaling relation from different datasets are listed in **Table 4.1**. In Farahi et al. (2019) and Hollowood et al. (2018),  $\lambda_{piv} = 70$ , so the difference in intrinsic scatter is not so much that they are not comparable.

Notably, the  $T_X - \lambda$  sample for DES Y3 (**Fig. 4.1**) differs from those for DES Y1 (**Fig. 4.2 (a)**; Farahi et al. (2019)) in that there are many more low-richness clusters in this sample. We find normalization  $\beta$  and residual scatter  $\sigma_{intr}$  values to be very similar to those from the DES Y1 sample and from the SDSS DR8 sample (**Table 4.1**). The slope  $\alpha$

$r_{2500} T_X - \lambda$ Scaling Relations				
Dataset	$\beta$	$\alpha$	$\sigma_{intr}$	Figure
DES Y3	$1.91 \pm 0.02$	$0.36 \pm 0.05$	$0.27 \pm 0.02$	4.1
DES Y1 (Farahi et al., 2019)	$1.65 \pm 0.05^*$	$0.56 \pm 0.09$	$0.260 \pm 0.032$	4.2(a)
SDSS DR8 (Hollowood et al., 2018)	$1.82 \pm 0.02$	$0.54 \pm 0.04$	$0.26 \pm 0.02$	4.2(b)

Table 4.1: Scaling relations for  $T_X - \lambda$  within the  $r_{2500}$  radius across multiple samples. Scaling relations are presented in the format  $\ln(y) = \alpha \ln(\lambda/\lambda_{piv}) + \beta$  where  $y$  is  $E(z)^{-2/3}kT_X$ . We compare our results from clusters which appear both in *Chandra* archival data and in the Dark Energy Survey Year 1 and the Sloan Digital Sky Survey Data Release 8. Values for  $\beta$  and  $\sigma_{intr}$  are consistent across all three samples, whereas the current DES Y3 value for  $\alpha$  differs significantly from those found in other samples. \*This value of  $\beta$  was listed in the form  $e^{\pi T|\lambda}$  and had to be converted into a format where it could be compared. The corresponding error on  $\beta = \ln(e^{\pi T|\lambda})$  was propagated using the Derivative Method, such that it could also be compared to those in this study and in Hollowood et al. (2018).

is somewhat shallower than those found for DES Y1 and SDSS DR8. Though the *Chandra* sample of DES Y1 data contains many less low-richness clusters, the sample which appears in DES Y1 and *XMM-Newton* archival data (Farahi et al., 2019) does have many more low richness clusters. For a joint *Chandra-XMM* sample found in DES Y1,  $\alpha = 0.62 \pm 0.04$  (Farahi et al., 2019) is even further from ours. In addition, the SDSS DR8 *Chandra* sample has many low-richness clusters (**Fig. 4.2 (b)**; Hollowood et al. (2018)), so we cannot simply explain away our differences in slope with a broader sample. This may change in future, however, because we have not yet looked into outliers in our sample. In particular, mispercolated clusters, or clusters which *redMaPPer* has incorrectly split into two or more separate clusters, have a tendency to flatten the slope of scaling relations and have not yet been accounted for. A full investigation of outliers will be conducted before results are published.

#### 4.2.2 $L_X - \lambda$ Scaling Relation

The  $L_X - \lambda$  scaling relation was fit using the same methods as the  $T_X - \lambda$  relation.  $L_X - \lambda$  was not fit for DES Y1, but it was fit in Hollowood et al. (2018) for the SDSS DR8 redMaPPer catalog. Fit parameters for the  $r_{2500}$   $L_X - \lambda$  scaling relation in both datasets are listed in **Table 4.2**, and our fit is shown in **Fig. 4.3**, where  $L_X$  is scaled by  $10^{44}$  ergs/s. As we can see from **Fig. 4.3** and **Fig. 4.4**, the DES Y3 and SDSS DR8 samples do find a similar  $\sigma_{intr}$ , though for DES Y3 we get a noticeably higher intercept and somewhat lower slope (**Table 4.2**). As with the  $T_X - \lambda$  scaling relation, a lower slope value could be due to outliers from mispercolations. In addition, redshift cuts have not yet been made on this sample. The most reliable redshift range for the Dark Energy Survey is  $0.2 < z < 0.65$ , so

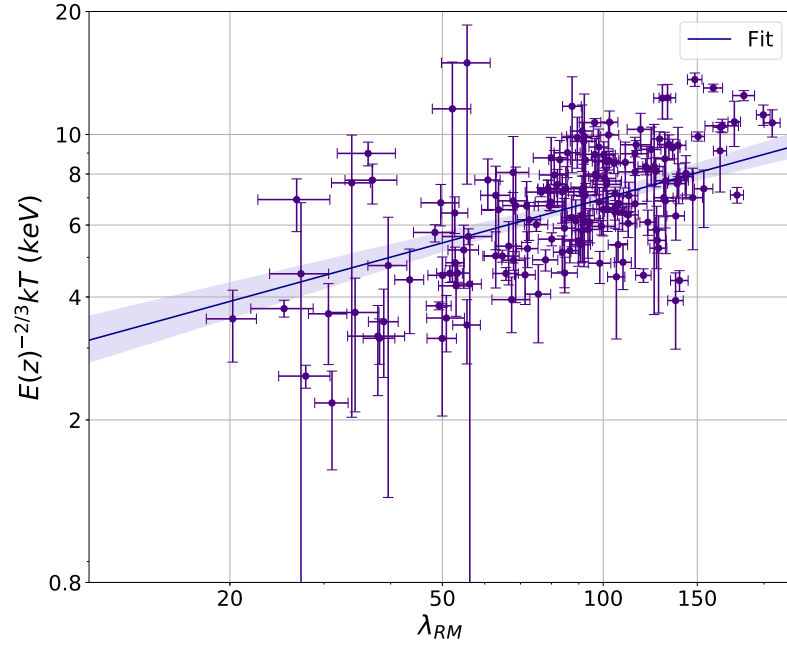


Figure 4.1: Preliminary  $r_{2500} T_X - \lambda$  scaling relation for DES Y3 clusters which appear in the *Chandra* archive. Purple points indicate cluster properties, where the blue line is the (fit) scaling relation. The fit line is surrounded by a translucent purple bar which denotes  $1\sigma$  error bars about the fit. The pivot point is the point at which this bar is lowest, at  $\lambda_{piv} = \lambda_{med} = 67.11$ .

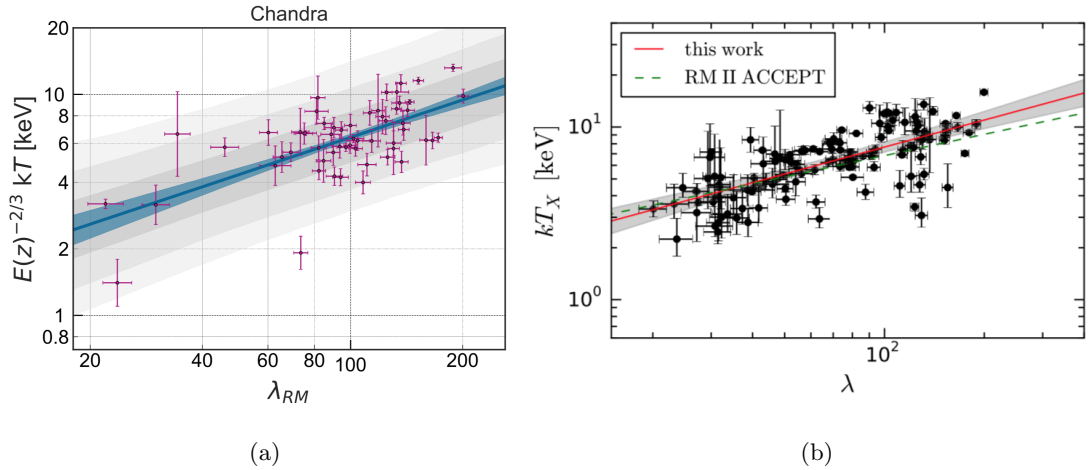


Figure 4.2: Previous results for  $r_{2500} T_X - \lambda$  scaling relations. (a) Sample from DES Y1 and *Chandra* archival data (Farahi et al., 2019). The purple points denote cluster data, while the blue line is the fit scaling relation. The blue bar around the fit is a  $1\sigma$  error about the fit. Each consecutive gray bar is another  $1\sigma$  of error from the fit. Note the comparative lack of low-richness clusters in this sample, and that the sample is much smaller than that of DES Y3 in general (**Fig. 4.1**). (b) Sample from SDSS DR8 and *Chandra* archival data (Hollowood et al., 2018). The black points mark cluster data, while the red line is the fit. The grey bar is a  $1\sigma$  error bar about the fit. The green dotted line is a scaling relation from Rozo & Rykoff (2014), which uses clusters from the SDSS DR8 *redMaPPer* catalog and the *Chandra* ACCEPT catalog; clusters which were selected for particularly deep *Chandra* observations.

$r_{2500} L_X - \lambda$ Scaling Relations				
Dataset	$\beta$	$\alpha$	$\sigma_{intr}$	Figure
DES Y3	$0.18 \pm 0.06$	$1.09 \pm 0.09$	$0.85 \pm 0.01$	4.3
SDSS DR8 (Hollowood et al., 2018)	$-0.08 \pm 0.05$	$1.37 \pm 0.08$	$0.84 \pm 0.03$	4.4

Table 4.2:  $L_X - \lambda$  scaling relations for the  $r_{2500}$  soft band luminosity across datasets. Scaling relations are presented in the format  $\ln(y) = \alpha \ln(\lambda/\lambda_{piv}) + \beta$  where  $y$  is  $L_X/E(z)$  and  $L_X$  has units of  $10^{44}$  ergs/s. We compare our results to those from Hollowood et al. (2018). Note that  $\sigma_{intr}$  is very similar, but  $\alpha$  and  $\beta$  differ between the samples.

our  $L_X - \lambda$  scaling relation for DES Y3 may change after additional cuts.

### 4.3 Centering

A centering histogram was made of scaled offsets between the X-ray peak of a cluster and its center according to *redMaPPer*. The offset is scaled by the richness radius  $R_\lambda = (\lambda/100)^{0.2} h^{-1} \text{Mpc}$  where  $h = H_0/100 \text{kms}^{-1} \text{Mpc}^{-1} = 0.7$ , which assumes a flat  $\Lambda$ CDM cosmology. This histogram was fit to two gamma functions using well-centered and mis-centered models and the same methods as in Zhang et al. (2019):

$$P(x|\rho, \sigma, \tau) = \rho \times P_{cent}(x|\sigma) + (1 - \rho) \times P_{miscent}(x|\tau) \quad (4.1)$$

where  $x = r_{offset}/R_\lambda$ ,  $P_{cent}(x|\sigma)$  and  $P_{miscent}(x|\tau)$  are the centered and mis-centered distributions, and  $\rho$ ,  $\sigma$  and  $\tau$  are fit parameters. We define

$$P_{cent}(x|\sigma) = \frac{1}{\sigma} \exp\left(-\frac{x}{\sigma}\right) \quad (4.2)$$

and

$$P_{miscent}(x|\tau) = \frac{x}{\tau^2} \exp\left(-\frac{x}{\tau}\right) \quad (4.3)$$

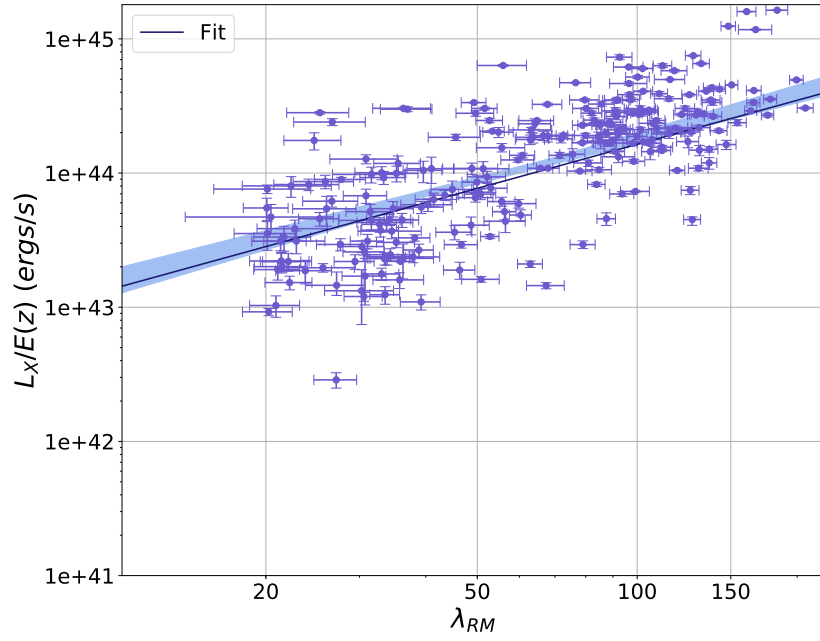


Figure 4.3: Preliminary  $r_{2500}$   $L_X - \lambda$  scaling relation for DES Y3 clusters in the *Chandra* archival sample. Lavender points are our data, where the blue line through the center is the scaling relation. This is surrounded by a lighter blue  $1\sigma$  error bar. The pivot point for this fit was  $\lambda = \lambda_{med} = 67.11$ .

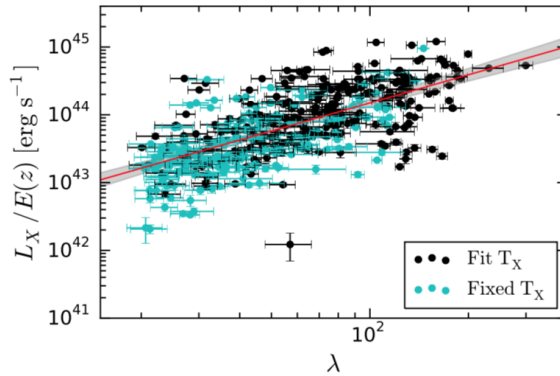


Figure 4.4:  $r_{2500} L_X - \lambda$  scaling relation from Hollowood et al. (2018). Black points indicate  $L_X$  values which were fit alongside  $T_X$ , and green points indicate  $L_X$  values which were fit with an assumed  $T_X$ . The red line is the fit, and the gray bar is a  $1\sigma$  error bar about the fit.

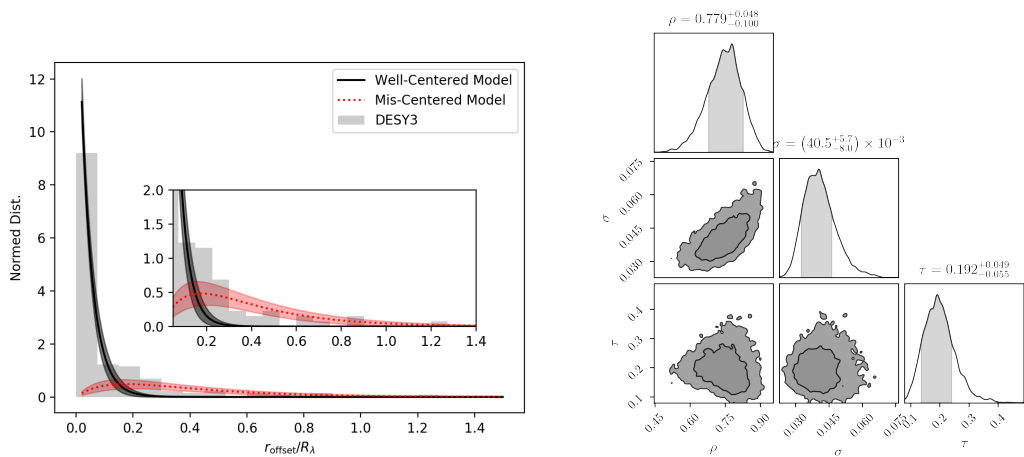
as in Zhang et al. (2019). The fit produced the distributions shown in **Fig. 4.5** and the parameters listed in **Table 4.3**. The parameter  $\rho$  represents the fraction of well-centered clusters. For the DES Y3 *redMaPPer* sample, the fraction of well-centered clusters was  $0.779^{+0.048}_{-0.100}$ , which is consistent within uncertainties for DES Y1 and SDSS DR8 (see **Table 4.3**).  $\tau$  is the width of the mis-centered distribution, or how offset the mis-centered clusters are. Our  $\tau$  value of  $0.192^{+0.049}_{-0.055}$  is consistent within uncertainty of DES Y1 and SDSS DR8 *redMaPPer* samples.  $\sigma$  represents the width of the well-centered distribution. This accounts for uncertainties in X-ray positions of clusters, as X-ray gas does not trace perfectly with number of cluster galaxies. Our  $\sigma = 0.0405^{+0.0057}_{-0.0080}$  for DES Y3 is consistent with  $\sigma$  for DES Y1.

Centering distribution parameters in DES Y3 vs. Y1 and SDSS DR8 samples.

Dataset	$\rho$	$\sigma$	$\tau$
DES Y3	$0.779^{+0.048}_{-0.100}$	$0.0405^{+0.0057}_{-0.0080}$	$0.192^{+0.049}_{-0.055}$
DES Y1 (Zhang et al., 2019)	$0.835^{+0.112}_{-0.075}$	$0.0443^{+0.0231}_{-0.0094}$	$0.166^{+0.111}_{-0.042}$
SDSS DR8 (Zhang et al., 2019)	$0.678^{+0.035}_{-0.051}$	$0.0156^{+0.0026}_{-0.0020}$	$0.179^{+0.021}_{-0.021}$

Table 4.3: Fit parameters for centering gamma distributions across *redMaPPer* catalogs.

All were fit using the methods in Zhang et al. (2019) for Bhargava et al. (*in prep*). The parameter  $\rho$  indicates the fraction of clusters in the sample which are well-centered.

Figure 4.5: Centering histogram and corner plot for DES Y3 data Bhargava et al. (*prep*).

The data are fit to two separate Gamma distributions, a “well-centered” model in black, and a “mis-centered” model in red. The inlaid plot shows a zoomed-in image of the area where the mis-centered histogram begins to dominate. The corner plot suggests that there is weak correlation between the fit parameters, but that they all follow roughly Gaussian distributions.

## 5

## Summary and Future Work

In this thesis, we present preliminary results for a *Chandra* X-ray follow up to the Dark Energy Survey Year 3 *redMaPPer* sample, as well as significant upgrades to the *MATCha* analysis pipeline. We implement X-ray analysis centered on cluster X-ray peaks, and develop iterative methods to find X-ray luminosities without temperatures which are consistent with  $r_{2500}$  band luminosities which are fit alongside temperatures. We find an  $r_{2500} T_X - \lambda$  relation of  $\ln(E(z)^{-2/3} kT_X) = (0.36 \pm 0.05) \ln(\lambda/67.11) + (1.91 \pm 0.02)$  ( $\sigma_{intr} = 0.28 \pm 0.02$ ) and an  $r_{2500} L_X - \lambda$  relation of  $\ln(L_X/E(z)) = (1.09 \pm 0.09) \ln(\lambda/67.11) + (0.18 \pm 0.06)$  ( $\sigma_{intr} = 0.85 \pm 0.01$ ). We find a well-centered fraction of  $0.779^{+0.048}_{-0.100}$ , which is consistent with previous analysis despite more than doubling the DES Y1 *redMaPPer*-selected sample in the *Chandra* archive. Quantifying the intrinsic scatter on the richness  $\lambda$  allows for better mass estimates of galaxy clusters, enabling more accurate cosmology from richness-mass relations. The cluster mis-centering distribution is an important systematic in cluster cosmology, and therefore our centering results also enable more accurate cosmology from clusters in DES Y3.

The first step in continuing this analysis is to investigate outliers in the scaling relation samples. Some outliers may be due to errors in *redMaPPer* or *MATCha* such as mispercolation, so corrections could meaningfully change results. Further data cuts on redshift, as well as recalculating richness at cluster X-ray peaks for DES Y3, should improve the accuracy of our scaling relations, so that they will be ready for publication. Analysis should be repeated on the  $r_{500}$  regions for DES Y3.

Further work with *MATCha* that directly follows from this thesis would be the completion of automated flagging code outlined **Section 3.3**. Preliminary implementation of chip-edge flagging is currently being worked on by Jose Jobel, an undergraduate in the research group, with my guidance. However, improved chip-edge flagging (which involves not just the fraction of “good” and “bad” pixels, but the distance of the nearest point in the source region to the edge of a *Chandra* CCD chip) could be attempted in future. From there, it would not be too complicated to automate flagging whether particular source regions ( $500\text{kpc}$ ,  $r_{2500}$ , and  $r_{500}$ ) were outside of a chip edge and should be excluded from analysis individually. This would be particularly valuable for clusters where the  $r_{500}$  radius extends past a chip edge but the  $r_{2500}$  radius does not. Other flagging (for example, flagging that *Chandra* is in spectroscopy mode at the time of the observation) could be automated as well.

Finally, the code outlined in **Section 3.2** should be used in analysis of core-cropped  $r_{500}$  regions. Though previous analyses of core-cropped  $r_{500}$  regions has been performed, centering those core-cropped regions on the centroid rather than the X-ray peak became problematic in cases where the centroid was offset from the cluster core. This should be ameliorated with the implementation of centering on the X-ray peak, and therefore should

result in lower-scatter  $L_X$  scaling relations.

The analysis detailed in this thesis will likely be repeated on the Dark Energy Survey Year 5 data release. Similar X-ray follow-up will likely be pertinent to cluster cosmology with the Large Synoptic Sky Telescope (LSST) using *redMaPPer*. In addition, there is no reason why the use of *MATCha* should be restricted to *redMaPPer* cluster catalogs in particular. *MATCha* could reasonably be expanded to accommodate any cluster catalog which includes a redshift estimate. Therefore, the use of *MATCha* in *Chandra* X-ray follow-up of optical clusters should endure through at least the next ten years.

# Bibliography

- Arnaud, M., Pointecouteau, E., & Pratt, G. W. (2005). The structural and scaling properties of nearby galaxy clusters. II. The M-T relation. *Astronomy and Astrophysics*, 441, 893–903.
- Bell, E. F., Wolf, C., Meisenheimer, K., Rix, H.-W., Borch, A., Dye, S., Kleinheinrich, M., Wisotzki, L., & McIntosh, D. H. (2004). Nearly 5000 Distant Early-Type Galaxies in COMBO-17: A Red Sequence and Its Evolution since  $z \sim 1$ . *The Astrophysical Journal*, 608, 752–767.
- Bhargava et al. (in prep.).
- Farahi, A., Chen, X., Evrard, A. E., Hollowood, D. L., Wilkinson, R., Bhargava, S., Giles, P., Romer, A. K., Jeltema, T., Hilton, M., Bermeo, A., Mayers, J., Cervantes, C. V., Rozo, E., Rykoff, E. S., Collins, C., Costanzi, M., Everett, S., Liddle, A. R., Mann, R. G., Mantz, A., Rooney, P., Sahlen, M., Stott, J., Viana, P. T. P., Zhang, Y., Annis, J., Avila, S., Brooks, D., Buckley-Geer, E., Burke, D. L., Rosell, A. C., Kind, M. C., Carretero, J., Castander, F. J., da Costa, L. N., De Vicente, J., Desai, S., Diehl, H. T., Dietrich, J. P., Doel, P., Flaughner, B., Fosalba, P., Frieman, J., García-Bellido, J., Gaztanaga, E., Gerdes, D. W., Gruen, D., Gruendl, R. A., Gschwend, J., Gutierrez, G., Honscheid,

- K., James, D. J., Krause, E., Kuehn, K., Kuropatkin, N., Lima, M., Maia, M. A. G., Marshall, J. L., Melchior, P., Menanteau, F., Miquel, R., Ogando, R. L. C., Plazas, A. A., Sanchez, E., Scarpine, V., Schubnell, M., Serrano, S., Sevilla-Noarbe, I., Smith, M., Sobreira, F., Suchyta, E., Swanson, M. E. C., Tarle, G., Thomas, D., Tucker, D. L., Vikram, V., Walker, A. R., & Weller, J. (2019). Mass Variance from Archival X-ray Properties of Dark Energy Survey Year-1 Galaxy Clusters. *arXiv:1903.08042 [astro-ph]*.
- Fruscione, A., McDowell, J. C., Allen, G. E., Brickhouse, N. S., Burke, D. J., Davis, J. E., Durham, N., Elvis, M., Galle, E. C., Harris, D. E., Huenemoerder, D. P., Houck, J. C., Ishibashi, B., Karovska, M., Nicastro, F., Noble, M. S., Nowak, M. A., Primini, F. A., Siemiginowska, A., Smith, R. K., & Wise, M. (2006). CIAO: Chandra's data analysis system. In *Society of Photo-Optical Instrumentation Engineers (SPIE) Conference Series*, volume 6270 (pp. 62701V).
- Hollowood, D. L., Jeltama, T., Chen, X., Farahi, A., Evrard, A., Everett, S., Rozo, E., Rykoff, E., Bernstein, R., Bermeo, A., Eiger, L., Giles, P., Israel, H., Michel, R., Noorali, R., Romer, K., Rooney, P., & Splettstoesser, M. (2018). Chandra Follow-Up of the SDSS DR8 redMaPPer Catalog Using the MATCha Pipeline. *arXiv:1808.06637 [astro-ph]*.
- Kaiser, N. (1991). Evolution of clusters of galaxies. *The Astrophysical Journal*, 383, 104–111.
- Kelly, B. C. (2007). Some Aspects of Measurement Error in Linear Regression of Astronomical Data. *The Astrophysical Journal*, 665, 1489–1506.
- Leauthaud, A., Finoguenov, A., Kneib, J.-P., Taylor, J. E., Massey, R., Rhodes, J., Ilbert, O., Bundy, K., Tinker, J., George, M. R., Capak, P., Koekemoer, A. M., Johnston, D. E., Zhang, Y.-Y., Cappelluti, N., Ellis, R. S., Elvis, M., Giodini, S., Heymans, C., Le Fèvre,

- O., Lilly, S., McCracken, H. J., Mellier, Y., Réfrégier, A., Salvato, M., Scoville, N., Smoot, G., Tanaka, M., Van Waerbeke, L., & Wolk, M. (2010). A Weak Lensing Study of X-Ray Groups in the Cosmos Survey: Form and Evolution of the Mass-Luminosity Relation. *The Astrophysical Journal*, 709(1), 97–114.
- Melchior, P., Gruen, D., McClintock, T., Varga, T. N., Sheldon, E., Rozo, E., Amara, A., Becker, M. R., Benson, B. A., Bermeo, A., Bridle, S. L., Clampitt, J., Dietrich, J. P., Hartley, W. G., Hollowood, D., Jain, B., Jarvis, M., Jeltama, T., Kacprzak, T., MacCrann, N., Rykoff, E. S., Saro, A., Suchyta, E., Troxel, M. A., Zuntz, J., Bonnett, C., Plazas, A. A., Abbott, T. M. C., Abdalla, F. B., Annis, J., Benoit-Lévy, A., Bernstein, G. M., Bertin, E., Brooks, D., Buckley-Geer, E., Carnero Rosell, A., Carrasco Kind, M., Carretero, J., Cunha, C. E., D’Andrea, C. B., da Costa, L. N., Desai, S., Eifler, T. F., Flaugher, B., Fosalba, P., García-Bellido, J., Gaztanaga, E., Gerdes, D. W., Gruendl, R. A., Gschwend, J., Gutierrez, G., Honscheid, K., James, D. J., Kirk, D., Krause, E., Kuehn, K., Kuropatkin, N., Lahav, O., Lima, M., Maia, M. A. G., March, M., Martini, P., Menanteau, F., Miller, C. J., Miquel, R., Mohr, J. J., Nichol, R. C., Ogando, R., Romer, A. K., Sanchez, E., Scarpine, V., Sevilla-Noarbe, I., Smith, R. C., Soares-Santos, M., Sobreira, F., Swanson, M. E. C., Tarle, G., Thomas, D., Walker, A. R., Weller, J., & Zhang, Y. (2017). Weak-lensing mass calibration of redMaPPer galaxy clusters in Dark Energy Survey Science Verification data. *Monthly Notices of the Royal Astronomical Society*, 469, 4899–4920.
- NASA/IPAC Extragalactic Database (2019). <https://ned.ipac.caltech.edu/>.
- Perlmutter, S., Turner, M. S., & White, M. (1999). Constraining Dark Energy with Type

- Ia Supernovae and Large-Scale Structure. *Physical Review Letters*, 83(4), 670–673.
- Riess, A. G., Filippenko, A. V., Challis, P., Clocchiatti, A., Diercks, A., Garnavich, P. M., Gilliland, R. L., Hogan, C. J., Jha, S., Kirshner, R. P., Leibundgut, B., Phillips, M. M., Reiss, D., Schmidt, B. P., Schommer, R. A., Smith, R. C., Spyromilio, J., Stubbs, C., Suntzeff, N. B., & Tonry, J. (1998). Observational Evidence from Supernovae for an Accelerating Universe and a Cosmological Constant. *The Astronomical Journal*, 116, 1009–1038.
- Rozo, E. & Rykoff, E. S. (2014). redMaPPer II: X-Ray and SZ Performance Benchmarks for the SDSS Catalog. *The Astrophysical Journal*, 783, 80.
- Rozo, E., Rykoff, E. S., Koester, B. P., McKay, T., Hao, J., Evrard, A., Wechsler, R. H., Hansen, S., Sheldon, E., Johnston, D., Becker, M., Annis, J., Bleem, L., & Scranton, R. (2009). Improvement of the Richness Estimates of maxBCG Clusters. *The Astrophysical Journal*, 703, 601–613.
- Rykoff, E. S., Rozo, E., Busha, M. T., Cunha, C. E., Finoguenov, A., Evrard, A., Hao, J., Koester, B. P., Leauthaud, A., Nord, B., Pierre, M., Reddick, R., Sadibekova, T., Sheldon, E. S., & Wechsler, R. H. (2014). redMaPPer I Algorithm and SDSS DR8 Catalog. *The Astrophysical Journal*, 785(2), 104.
- Rykoff, E. S., Rozo, E., Hollowood, D., Bermeo-Hernandez, A., Jeltama, T., Mayers, J., Romer, A. K., Rooney, P., Saro, A., Cervantes, C. V., Wechsler, R. H., Wilcox, H., Abbott, T. M. C., Abdalla, F. B., Allam, S., Annis, J., Benoit-Lévy, A., Bernstein, G. M., Bertin, E., Brooks, D., Burke, D. L., Capozzi, D., Rosell, A. C., Kind, M. C., Castander, F. J., Childress, M., Collins, C. A., Cunha, C. E., D’Andrea, C. B., da Costa,

- L. N., Davis, T. M., Desai, S., Diehl, H. T., Dietrich, J. P., Doel, P., Evrard, A. E., Finley, D. A., Flaugher, B., Fosalba, P., Frieman, J., Glazebrook, K., Goldstein, D. A., Gruen, D., Gruendl, R. A., Gutierrez, G., Hilton, M., Honscheid, K., Hoyle, B., James, D. J., Kay, S. T., Kuehn, K., Kuropatkin, N., Lahav, O., Lewis, G. F., Lidman, C., Lima, M., Maia, M. A. G., Mann, R. G., Marshall, J. L., Martini, P., Melchior, P., Miller, C. J., Miquel, R., Mohr, J. J., Nichol, R. C., Nord, B., Ogando, R., Plazas, A. A., Reil, K., Sahlén, M., Sanchez, E., Santiago, B., Scarpine, V., Schubnell, M., Sevilla-Noarbe, I., Smith, R. C., Soares-Santos, M., Sobreira, F., Stott, J. P., Suchyta, E., Swanson, M. E. C., Tarle, G., Thomas, D., Tucker, D., Uddin, S., Viana, P. T. P., Vikram, V., Walker, A. R., Zhang, Y., & The DES Collaboration (2016). The redMaPPer Galaxy Cluster Catalog from DES Science Verification Data. *The Astrophysical Journal Supplement Series*, 224(1), 1.
- Simet, M., McClintock, T., Mandelbaum, R., Rozo, E., Rykoff, E., Sheldon, E., & Wechsler, R. H. (2017). Weak lensing measurement of the mass-richness relation of SDSS redMaPPer clusters. *Monthly Notices of the Royal Astronomical Society*, 466, 3103–3118.
- The Dark Energy Survey Collaboration (2005). The Dark Energy Survey. *arXiv:astro-ph/0510346*.
- Vikhlinin, A., Kravtsov, A., Forman, W., Jones, C., Markevitch, M., Murray, S. S., & Van Speybroeck, L. (2006). Chandra Sample of Nearby Relaxed Galaxy Clusters: Mass, Gas Fraction, and Mass-Temperature Relation. *The Astrophysical Journal*, 640, 691–709.
- Vikhlinin, A., Kravtsov, A. V., Burenin, R. A., Ebeling, H., Forman, W. R., Hornstrup, A., Jones, C., Murray, S. S., Nagai, D., Quintana, H., & Voevodkin, A. (2009). Chandra

Cluster Cosmology Project III: Cosmological Parameter Constraints. *The Astrophysical Journal*, 692, 1060–1074.

Zhang, Y., Jeltema, T., Hollowood, D. L., Everett, S., Rozo, E., Farahi, A., Bermeo, A., Bhargava, S., Giles, P., Romer, A. K., Wilkinson, R., Rykoff, E. S., Mantz, A., Diehl, H. T., Evrard, A. E., Stern, C., Gruen, D., von der Linden, A., Splettstoesser, M., Chen, X., Costanzi, M., Allen, S., Collins, C., Hilton, M., Klein, M., Mann, R. G., Manolopoulou, M., Morris, G., Mayers, J., Sahlen, M., Stott, J., Cervantes, C. V., Viana, P. T. P., Wechsler, R. H., Allam, S., Avila, S., Bechtol, K., Bertin, E., Brooks, D., Burke, D. L., Rosell, A. C., Kind, M. C., Carretero, J., Castander, F. J., da Costa, L. N., De Vicente, J., Desai, S., Dietrich, J. P., Doel, P., Flaughner, B., Fosalba, P., Frieman, J., García-Bellido, J., Gaztanaga, E., Gruendl, R. A., Gschwend, J., Gutierrez, G., Hartley, W. G., Honscheid, K., Hoyle, B., Krause, E., Kuehn, K., Kuropatkin, N., Lima, M., Maia, M. A. G., Marshall, J. L., Melchior, P., Menanteau, F., Miller, C. J., Miquel, R., Ogando, R. L. C., Plazas, A. A., Sanchez, E., Scarpine, V., Schindler, R., Serrano, S., Sevilla-Noarbe, I., Smith, M., Soares-Santos, M., Suchyta, E., Swanson, M. E. C., Tarle, G., Thomas, D., Tucker, D. L., Vikram, V., & Wester, W. (2019). Dark Energy Survey Year 1 Results: Calibration of Cluster Mis-centering in the redMaPPer Catalogs. *arXiv:1901.07119 [astro-ph]*.